

# Chapter 1

## Strong-Field Induced Atomic Excitation and Kinematics

U. Eichmann

**Abstract** Frustrated tunneling ionization (FTI) has recently been found to be an important exit channel of atomic strong-field ionization models such as the simple man's or rescattering model if one considers the Coulomb field explicitly. It leads to the population of bound excited states rather than to ionization after the electron has tunneled and quivered in the laser field. In this chapter we introduce the FTI model and describe experiments whose outcome supports its importance. In particular, we focus on strong-field excitation of atoms and the observation of neutral (ionic) excited fragments with high kinetic energy in strong-field fragmentation and Coulomb explosion of small molecules. Furthermore, we present experiments in which a direct position sensitive detection of excited neutral atoms reveals the exceptionally high acceleration of atoms in short pulsed strongly focused laser fields and discuss possible applications.

### 1.1 Introduction

The understanding of strong-field ionization dynamics of atoms and molecules rests a great deal on the seminal tunneling picture introduced by Keldysh [1]. A linearly polarized pulsed strong laser field is considered as a classical electric field  $\mathbf{F}(t) = \mathbf{F}_L(t) \cos(\omega t)$  with  $\mathbf{F}_L(t) = f(t) F_0 \hat{\mathbf{e}}_x$ , where  $f(t)$  is a slowly time-varying pulse envelope,  $F_0$  is the field amplitude and  $\omega$  is the angular frequency of the laser. All equations throughout the paper are given in atomic units unless otherwise stated. If an atom in its ground state with an ionization potential  $I_P$  is exposed to such a laser field, the atomic Coulomb potential is periodically bent up and down and allows for tunneling of an electron at certain phases of the laser field. The pure tunneling picture describes ionization extremely well, particularly in those situations, where a fairly large number of photons is necessary to overcome the binding energy. The Keldysh parameter  $\gamma = \sqrt{I_P/2U_p}$ , where  $U_p = F^2/4\omega^2$  is the ponderomotive potential, is

---

U. Eichmann (✉)

Max-Born-Institute, Max-Born-Strasse 2a, 12489 Berlin, Germany  
e-mail: eichmann@mbi-berlin.de

used to distinguish the tunneling regime  $\gamma < 1$  from the multiphoton regime  $\gamma > 1$ . It has been found, however, that the subsequent dynamics of the electron in the laser field is of decisive importance. It results in secondary processes, which are embraced in the simple man's model [2–4] and in the famous three-step or rescattering model [5–7]. The simple man's model concentrates on the cycle-averaged energy a liberated electron can extract from the classical laser field, neglecting any interaction with the parent ion in the first place. The rescattering model, on the other hand, focuses on the processes initiated after the first return(s) of the electron to the core, where particularly electrons liberated in a certain phase range after a field cycle maximum provide high kinetic energies at the return. These processes include high-order above threshold ionization (HATI) [8], non-sequential double or non-sequential multiple-ionization (NSDI) by collision [9–12] and radiative recombination generating high harmonics (HHG) [13, 14].

We will concentrate on the dynamics of electrons, which tunnel around the field cycle maximum thus avoiding substantial energy transfer during rescattering with the parent ion. Astonishingly, the physical consequences that arise in the context of these electrons have not been considered coherently before, neither in the simple man's model nor in the rescattering model. By taking into account the Coulomb field explicitly, one finds that ionization of the atom, expected to follow the tunneling process of the electron, is frustrated under certain circumstances. This exit channel leads to the population of excited states. The process, which has been dubbed frustrated tunneling ionization (FTI), describes quantitatively (quasi multi-photon) excitation within the tunneling picture [15].

To put the FTI model into perspective one has to mention that since the early days of optical strong-field physics, experiments have shown beside multiphoton ionization also multiphoton excitation [16–19]. In the multiphoton picture, it was argued qualitatively that a Rydberg state is excited at the beginning of the laser pulse. Similar to a free electron the quasi free Rydberg electron does not absorb energy from the electromagnetic field and remains bound. The picture of Rydberg state excitation was strongly supported by the observation of strong enhancements in the above threshold ionization (ATI) electron spectra, which were explained in terms of transient Freeman resonances [20]. These are Rydberg states that are shifted ponderomotively into resonance with the laser field at particularly intensities during the rise of the laser pulse and subsequently ionized. To explain why an atom in a Rydberg state is finally stable against ionization, different stabilization mechanisms [21] such as interference stabilization at lower intensities [22–27] or strongly reduced ionization rates due to high angular momentum [17, 28] have been suggested. An easy quantitative explanation of excitation in the multiphoton picture, however, has not been achieved.

We remark that population trapping in excited states should not be misinterpreted with atomic stabilization in strong laser fields. Simply speaking the strong-field actually stabilizes the atom by reducing the overlap of the laser driven electronic wave function with the ionic core. This phenomenon, usually associated with the situation that a single-photon absorption is in principle sufficient to ionize, was first predicted about a quarter century ago [29–32]. Since then, the subject has been extensively

discussed theoretically for the last two decades [33, 34] with newly increased interest [35, 36]. Stabilization of a single prepared low lying Rydberg state in a moderately strong laser field without any remaining loop holes such as state redistribution has been observed in impressive experiments [37, 38].

The qualitative arguments expressed within the multiphoton picture were also applied to explain excitation of atoms in the strong-field tunneling regime. In [18, 39] high-lying Rydberg states after strong-field interaction were observed by subsequent field ionization and in [40], e.g., excitation was deduced from structures in the measured ionization yields. First trials to explain excitation in the strong-field tunneling regime have been given within the simple man's model [2–4]. Early investigations on stabilization of atoms using classical Monte Carlo analysis [41] found as an alternate way to stabilization that the quivering electrons land on Rydberg states after the laser pulse has terminated. Yudin and Ivanov reported transient Rydberg trajectories [42] in the tunneling regime and finally Muller concluded from extensive quantum mechanical calculation excitation in the tunneling regime [43]. Only recently excited states of He have been observed [15], in which the intensities were well in the tunneling regime of strong-field physics. The obvious question that arose in this context was whether there is a way to comprehend strong-field excitation purely within the tunneling picture without invoking the multiphoton picture. The solution lies in the frustrated tunneling ionization model, which describes astonishingly well observed features.

In the following sections we will elucidate in detail how frustrated tunneling ionization leads to excited states and we will discuss consequences for strong-field physics. Besides important ramifications in atomic strong-field physics we also find FTI at work in strong-field dissociation of molecules. Finally, FTI establishes the basis to explain observed kinematic effects of strong inhomogeneous fields on neutral atoms.

## 1.2 Strong Field Excitation of Atoms by Frustrated Tunneling Ionization (FTI)

### 1.2.1 Linearly Polarized Laser Fields

In tunneling models, the tunneling process is mostly regarded to be tantamount to tunneling ionization. This is correct, if no attractive potential, whatsoever, is explicitly considered in the first place. However, by taking into account the Coulomb potential of the parent ion, frustrated tunneling ionization might happen. Assuming that the tunneling process is instantaneous at some time  $t_t$ , the electron is then located at the tunnel exit, which is only a few Bohr radii away from the ionic core. At this point, the electron has a high negative potential energy of a few eV. The electron quivers in the strong laser field and, whenever the tunneled electron does not gain enough energy during the interaction with both the laser field and the Coulomb field to finally

overcome the attractive Coulomb force [15], it has not been set free at all. Therefore, one expects FTI to occur mainly for electrons that tunnel in the vicinity of a field cycle maximum of a linearly polarized laser field at a phase  $\phi_t = \omega t_t \approx 0$  (or a multiple integer of  $\pi$ ). In this case, the laser induced drift energy, given by  $E_{dr} = 2U_p \sin^2 \phi_t$  [19], is close to zero and also the energy upon the first rescattering on the parent ion is rather moderate and typically less than the potential energy in the Coulomb field.

Decisive, whether ionization occurs after tunneling, or not, is the total energy  $T$  of the electron at a time, when the laser pulse is over. If it is positive, the electron motion is eventually unbound, if it is negative, the electron will firmly relax into a bound state. Again, the notion in the rescattering model that the “electron tunnel ionizes in the first step” is correct as long as no attractive potential is considered. In the presence of an attractive potential one can assert that ionization has happened only after the laser pulse is over. Consequently, thinking in terms of the rescattering model, where it is common agreement that an electron is considered to be “ionized” after the tunneling process, the term frustrated tunneling ionization is meaningful and justified. However, it is most important to emphasize that an electron that has undergone frustrated tunneling ionization, has in fact never been unbound in the sense of a strict definition of ionization.

In the following we will explore the parameter range for producing bound excited states through FTI. For given laser pulse parameters and a specified atom, which will be Helium in the present examples, the position and momentum of the electron, and the phase  $\phi_t$  of the oscillating laser field at the instant of tunneling are crucial [15, 44]. To calculate trajectories leading to frustrated tunneling ionization we solve the classical Newton equations for an electron in a combined pure Coulomb potential  $V_c(r) = -1/r$ , where  $r = \sqrt{x^2 + y^2 + z^2}$ , and the electric field  $\mathbf{F}(t)$ .

$$\ddot{\mathbf{x}}(t) = -\mathbf{F}(t) - \nabla V_c(r(t)) \quad (1.1)$$

The initial conditions at  $t_t$  are obtained from the tunneling ionization model, which locate the tunneling exit in a linearly polarized laser field at  $x(t_t) = -(I_p + [I_p^2 - 4|F(t_t)|]^{1/2})/2F(t_t)$ , and  $y(t_t) = z(t_t) = 0$ . Furthermore, at  $t_t$ , the longitudinal momentum of the electron along the polarization axis is  $p_x(t_t) = 0$ . The initial momentum perpendicular to the field axis  $p_\perp(t_t) = \sqrt{p_y^2 + p_z^2}$  is a parameter. To get an overview over bound and unbound trajectories we exploit the fact that trajectories are planar and symmetric with respect to the field axis. We thus vary  $p_y$  and take  $p_z = 0$ .

In Fig. 1.1 we show the occurrence of bound trajectories as a function of the parameters  $\phi_t = \omega t_t$  and  $p_y$ . For clarity we restrict the electron to tunnel only in the vicinity of the field cycle maximum at the laser pulse envelope maximum. The calculations are performed with a linearly polarized laser pulse with 8 fs (FWHM) pulse duration and field strengths of  $F_0 = 0.0755$  a.u. and  $F_0 = 0.169$  a.u., Fig. 1.1a, b, respectively, and with 29 fs (FWHM) pulse duration and the same field strengths as before, Fig. 1.1c, d, respectively. The Keldysh parameters associated with the two field strengths are  $\gamma = 1$  and  $\gamma = 0.44$ , respectively. Obviously, there are only

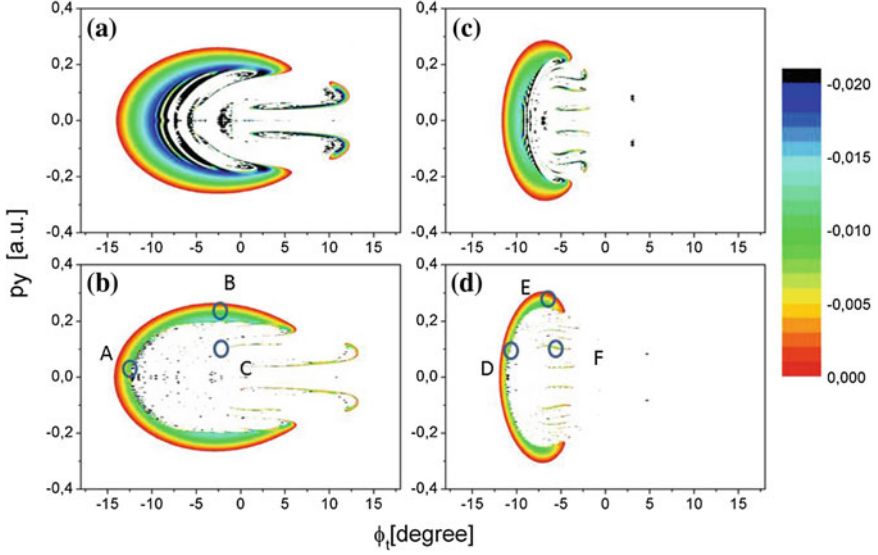


**Fig. 1.1** Occurrence of bound states after tunneling. Laser parameters:  $F_0 = 0.0755$  a.u. ( $2 \times 10^{14}$  W cm $^{-2}$ ) and **a** 8 fs (FWHM) and **b** 29 fs (FWHM) pulse duration. Laser parameters:  $F_0 = 0.169$  a.u. ( $10^{15}$  W cm $^{-2}$ ) and **c** 8 fs and **d** 29 fs pulse duration. The *circles* indicate initial parameters for calculated trajectories shown in Fig. 1.2. The phase  $\phi_t = \omega t_t$  is indicated with respect to the field cycle maximum at the maximum of the laser pulse envelope. Final negative total energy  $T$  of the electron is color coded. *White areas* stand for trajectories with positive total energy corresponding to strong-field ionization

certain well defined regions of the parameters, where frustrated tunneling ionization prevails. Inspecting Fig. 1.1a, b one finds that the parameter space for bound trajectories is much larger for electrons starting before the maximum than for electrons starting after it. Particularly, for the short laser pulses, Fig. 1.1a, one finds a relatively large region of parameters allowing for bound states [44]. In this case the laser drift momentum the electron acquires is opposite to the Coulomb force. If the electron starts after the field cycle maximum, the recollision with the ionic core is likely, which obviously counteracts formation of bound states. At longer pulse duration, Fig. 1.1b, on the other hand, the allowed parameter range is reduced and is characterized by distinct isolated areas. Apparently, bound states are no longer populated due to the higher probability of a fatal encounter of the electron with the ionic core at longer pulse durations. If we increase the field amplitude and use otherwise identical laser parameters, the parameter space for bound trajectories shrinks substantially, Fig. 1.1c, d. Most striking is that bound states are no longer found for electrons that tunnel after the field cycle maximum.

The interesting question that arises is how important is the influence of the Coulomb potential on the electron dynamics during the laser pulse? It is well known that most of the strong-field physics associated with the rescattering model

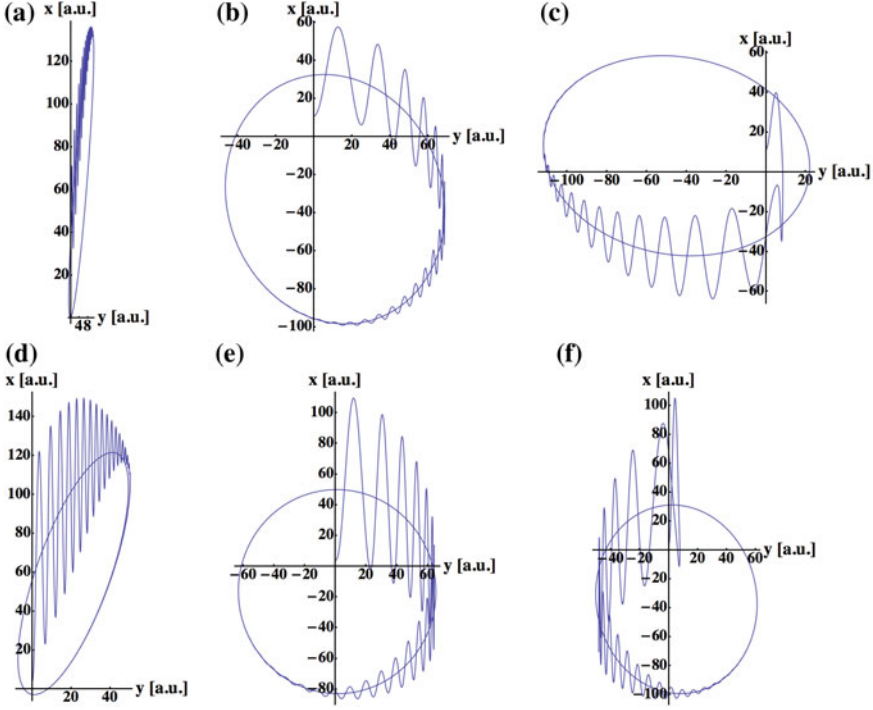


Fig. 1.2 Selected trajectories for initial conditions indicated in Fig. 1.1

is well described without invoking the Coulomb potential. To shed more light on the dynamics, it is very instructive to visualize and study electron trajectories at specific  $(\phi_t, p_y)$  parameters. We show different trajectories along an energy contour line with  $E_b \approx -7.8 \times 10^{-3}$  a.u. corresponding to roughly a principal quantum number  $n = 8$ . The initial conditions for trajectories shown in Fig. 1.2a–c are indicated in Fig. 1.1b by A–C, resp., and the initial conditions for trajectories shown in Fig. 1.2d–f are indicated in Fig. 1.1d by D–F, resp. The trajectories are calculated for several revolutions, so that the wiggly motion at early times during the laser pulse superimposes the final bound orbit at later times.

Trajectories, shown in (a) and (d), and in (b) and (e), were calculated using similar initial conditions, respectively. However, the quiver amplitude has more than doubled in (b) and (d), as expected for the higher field strength. In (a) and (c) the final bound orbits are oriented along the laser polarization with low angular momentum owing to the low initial perpendicular momentum. The role of the Coulomb field is important and by no means negligible, since the maximum excursion of the electron after the laser pulse is smaller than expected on the basis of a Coulomb field free motion. The same is true for the orbits shown in Fig. 1.2b, e. Here, the drift motion solely due to the laser field is weak, so that the electron is dominantly under the influence of the strong Coulomb field. Furthermore, the quiver motion averaged over one

laser period follows astonishingly well the final Coulomb orbit almost right from the start indicating that the Coulomb potential plays a significant role at each stage of the orbit. In Fig. 1.2c we show a trajectory, where the tunneling process started after the field cycle maximum so that the laser drift momentum pushes the electron initially towards the core. It is obvious that in this case the average over the wiggly trajectory at short times does not follow the orbital motion, but due to the close encounter with the ionic core the electron uses a complicated shortcut at some point, before it behaves regularly again. Overall, the bound orbits on an isoenergy shell behave regularly. They show a decrease of the eccentricity  $e$  of the orbit equivalent to an increase in angular momentum  $l$ , with increasing initial lateral momentum. Orbits calculated with parameters of isolated areas in the parameter space around the field cycle maximum show initially strongly irregular behavior. The occurrence of bound trajectories with initial parameters taken from the inner parameter space region strongly depends on the number of laser cycles following the tunneling event, as the electron dynamics is dominated by strong rescattering at the core. This is reflected in irregular behavior during the laser pulse, before the orbit finally merges into a stable orbit, as can be seen in Fig. 1.2f.

To summarize the semiclassical analysis, we conclude that the population of bound excited states stems from an interplay of the Coulomb field and the laser field on equal footing. Often, the averaged motion of the electron during the laser pulse follows already nicely the trajectory of the final orbit it will merge into. Consequently, any approximation of the Coulomb interaction during the laser field is not a priori justified. Although the Coulomb field influences the overall trajectory decisively, the amplitude of the electron's quiver motion seems to be still in accord with the assumption of a quasi free electron quivering in the laser field.

To calculate the yield of excited states one has to consider the probability for tunneling of an electron in the ground state with the magnetic quantum number  $m = 0$ , which is given within the simplest approximation of the tunneling model by [42, 45, 46]

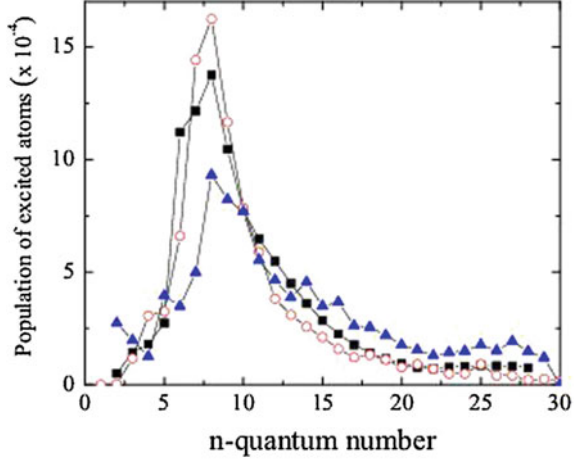
$$w_0 \propto \left( \frac{2(2I_P)^{3/2}}{|F(t_t)|} \right)^{\left( \frac{2}{\sqrt{2I_P}} - 1 \right)} \exp \left[ -2(2I_P)^{3/2}/3 |F(t_t)| \right]. \quad (1.2)$$

The probability to find a certain lateral momentum is given by [45]

$$w_{\perp} \propto \exp \left[ -p_{\perp}^2 \sqrt{2I_P} / |F(t_t)| \right]. \quad (1.3)$$

In semiclassical Monte-Carlo simulations one uses (1.2) and (1.3) to randomly pick initial conditions and start typically about  $10^5$ – $10^6$  trajectories. The total energy  $T = p(t_{fin})^2/2 + V(r(t_{fin}))$  of each trajectory is evaluated at time  $t_{fin}$  shortly after the laser pulse is over. As an example, we evaluate trajectories for He exposed to a laser field with intensities between ( $10^{14}$  and  $10^{15}$  W cm $^{-2}$ ) and a laser pulse duration ( $\tau = 27$  fs). We find  $\approx 10\%$  of all launched trajectories to be bound at the lower

**Fig. 1.3**  $n$  distribution of the population of excited states from a MC simulation (*red circle*), a quasi-one-electron (*black square*) and a full two-electron quantum mechanical calculation (*blue triangle*) at a laser intensity  $10^{15} \text{ W cm}^{-2}$ . The MC simulation has been normalized to the quasi-one-electron calculation at  $n = 10$ . From [15]



intensity  $10^{14} \text{ W cm}^{-2}$  and  $\approx 2.5\%$  at  $10^{15} \text{ W cm}^{-2}$ , see Fig. 1 of [15], confirming the FTI process to be an important exit channel.

One can then assign an effective quantum number  $\nu$  to each trajectory with negative total energy, determined by the Rydberg formula  $T = -1/2\nu^2$ . By sorting the effective quantum numbers into integer bins one obtains an  $n$  distribution, as shown in Fig. 1.3 and which is taken from [15]. The maximum of the distribution is around  $n = 8$  and the probability drops steeply towards both sides, but allowing for Rydberg states with higher  $n$  quantum numbers. An analysis of the classical angular momentum reveals that for states with  $n < 9$ , the probability to find a specific angular momentum within a fixed  $n$  shell increases strongly towards the maximum allowed value of  $l = n - 1$ . For larger  $n$  states, we find the same distribution with no angular momentum states higher than  $l = 9$ .

It is also instructive to look at the wavelength dependence of the yield of bound states. The drift energy and the quiver amplitude both scale  $\propto \omega^{-2}$  at constant laser intensity. Consequently, for shorter wavelengths the range of the parameter space for bound states increases and, with it, also the number of surviving trajectories. Particularly, population of lower  $n$  states with low radial extension benefits from the reduced quiver amplitude. On the other hand, increasing the wavelength results in the opposite behavior. Due to higher drift energy and a larger quiver motion, the parameter space for allowed trajectories shrinks and only bound trajectories with sufficient radial extension survive. The number of atoms surviving in lower  $n$  states is strongly diminished, while the number of atoms in higher  $n$  states remains the same. Consequently, the percentage of surviving atoms decreases. Finally, we mention that the FTI mechanism should also be in effect for strong-field excitation of ionic systems, see also Sect. 1.3.3.

The distribution shown in Fig. 1.3 has been confirmed by Monte-Carlo simulations of other groups [44, 47]. Most astounding, however, is the outcome of a direct comparison of the FTI results with TDSE calculations. In [15] the classical pre-

dictions were compared with results using the single-active electron (SAE) model and a full two-electron calculation, performed in the group of A. Saenz. The composition of the resulting Rydberg wave packet is in striking agreement, Fig. 1.3. The results demonstrate the predictive power of the frustrated tunneling ionization model. Similar results for the  $n$  distribution for different atoms and conditions have been obtained from other TDSE calculations [48–51] showing a maximum in the vicinity of  $n = 8$ . Only recently, we succeeded in measuring the  $n$  distribution by using a state selective field ionization method on the surviving neutral excited atoms. The results nicely confirm the theoretical predictions [52].

### 1.2.2 Elliptically Polarized Laser Fields

So far, we have described the FTI process in linearly polarized laser light. Hereby, most electrons tunnel in the vicinity of the field cycle maximum, so that the associated laser induced drift energy  $E_{dr} \approx 0$ . In an elliptically polarized laser field given by

$$\mathbf{F}(t) = F_0 f(t) (\cos(\omega t) \hat{\mathbf{e}}_x + \epsilon \sin(\omega t) \hat{\mathbf{e}}_y) / \sqrt{1 + \epsilon^2}, \quad (1.4)$$

however, an additional laser induced drift momentum in  $y$  direction (lateral direction) arises, which reads for  $\phi_t \approx 0$   $p_{dr,y} = -\epsilon F_0 / \omega \sqrt{\epsilon^2 + 1}$ .  $p_{dr,y}$ , and thus the total drift energy, are always nonzero for electrons that tunnel at  $\phi_t \approx 0$  and increase strongly with ellipticity  $\epsilon$ . It is this strong drift momentum that reduces substantially the population of bound states in elliptically polarized light. To include the polarization dependence, one might require in a simple approach that  $p_{dr,y}$  must be compensated by an appropriate initial lateral momentum,  $p_{\perp} = -p_{dr,y}$  to obtain bound states. Inserting this into (1.3),  $w(\epsilon)$  is then given by [53]

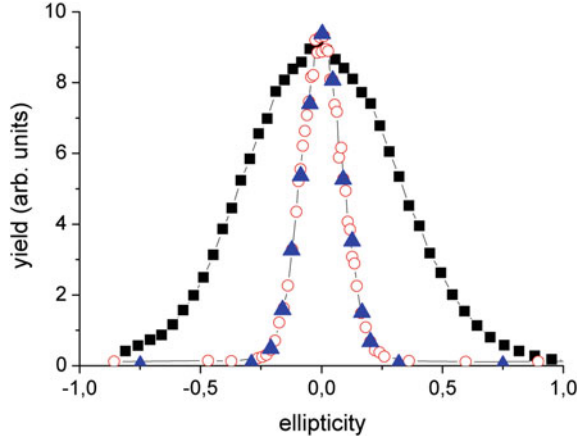
$$w(\epsilon) \approx \exp - \frac{F_0 (2I_p)^{1/2}}{\omega^2} \epsilon^2. \quad (1.5)$$

The results of this equation are in very good agreement with the experiment [15], which measured the total excited neutral yield as a function of ellipticity as shown in Fig. 1.4. We note that more extensive results have been obtained [47, 53] by solving (1.1) with the elliptically polarized laser field (1.4).

### 1.2.3 Intermediate Conclusion

The systematic investigation of electron trajectories emerging in a time window around a field cycle maximum revealed that the explicit inclusion of the Coulomb field in the rescattering model or simple man's model leads to bound states. Although bound or transient bound electron trajectories have been displayed occasionally in

**Fig. 1.4** Dependence of the  $\text{He}^+$  (black square) and  $\text{He}^*$  (red circle) yield on the ellipticity at fixed laser intensity of  $10^{15} \text{ W cm}^{-2}$ . For better comparison the height of both measurements have been set equal at  $\epsilon = 0$ , from [15]. Theoretical data points (blue triangle) are taken from [53]



the literature, the systematic study has shaped a clear picture of excitation in the tunneling regime. The FTI model also facilitates the interpretation of more complex experiments involving bound states and has led to a simple way to make quantitative predictions, in particular on the total yield of bound states and their  $n$  distribution. The FTI process shows qualitatively a similar behavior on ellipticity as the rescattering related processes HHG, NSDI, and HATI. In the latter cases, however, elliptical polarization reduces the rescattering probability with the ionic core, while in the FTI process formation of bound states is suppressed due to the high drift momentum. Nevertheless, one can consider the FTI process as a relevant additional exit channel in the rescattering model. It is important to note that if one uses the correct definition of the term ionization, which has no strict meaning unless the laser pulse is off, an atom finally in a bound excited state has never become ionized in the first place. This, in turn, implies that the process is not a classical electron recombination process involving emission of radiation as has been misleadingly argued occasionally in the literature [49, 50].

#### 1.2.4 Detection of Excited Atoms

The most prominent detection schemes in strong-field physics involve electron and ion detection by means of time of flight (TOF) techniques, velocity map imaging (VMI) [54], or a reaction microscope [55], as well as detection of high harmonic radiation. Usually, excited states of an atom are detected by subsequent photoionization or state selective field ionization, occasionally also by fluorescence measurements. In the scope of the present investigations experiments are based on a direct measurement. In Fig. 1.5 the sketch of an experimental setup shows how it is realized.

A well collimated thermal effusive beam of atoms, which is directed towards a position-sensitive multichannel plate (MCP) detector, is crossed by an intense

focused laser beam. Charged particles created by the laser-matter interaction can be refrained from reaching the detector by means of small electric fields. Excited and ground state atoms reach the detector after a mean time of flight that is determined by the drift distance  $d$  to the detector, the temperature and the mass of the atoms (for He atoms at room temperature with  $d = 0.38$  m it is  $\approx 200 \mu\text{s}$ ). The detector, however, is only able to detect excited atoms with sufficient internal energy. Considering the comparably long time of flight, radiative decay and black-body induced redistribution of the initial excited state distribution is unavoidable. Although the decay to the ground state is dominant, especially for low  $n$  and low  $l$  states, a substantial fraction of atoms decays to long-lived metastable states present in all rare gas atoms. Thus, an efficient detection is assured [52].

Without additional forces, as they will be discussed in Sect. 1.4.1, one expects to measure a pattern reflecting the excited atom probability distribution in the laser beam. While the radial dimension of the Gaussian laser beam is only on the order of the beam waist of a few tens of  $\mu\text{m}$ , which is small compared to the extension in laser beam direction on the order of the Rayleigh length of a few mm, excitation occurs within an elongated cylindrical volume along the laser beam axis. This is projected onto the detector, as can be seen for a measurement of excited  $\text{Ar}^*$  atoms hitting the detector, see Fig. 1.5a. Furthermore, neutral excited atom detection furthermore allows for a partially position dependent analysis of frustrated ionization dynamics within the focused volume. As will be discussed in Sect. 1.3, the detection technique allows also for the study of excited neutral atomic fragments from a strong-field dissociation process. Excited neutral fragment detection is well known in molecular physics, but has only been introduced in strong-field physics recently. The kinetic energy of the fragments is typically much higher than in an effusive beam, thus reducing the time of flight substantially. Consequently, excited states can be detected more likely in their initially populated states.

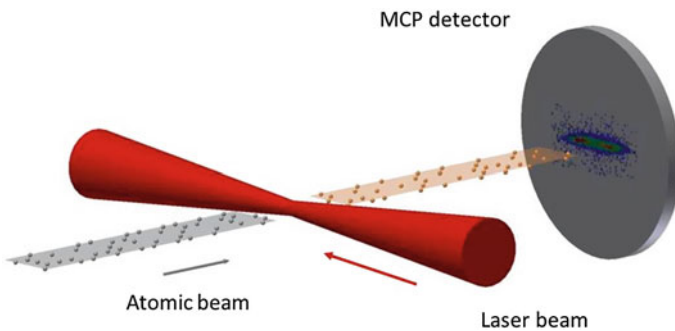
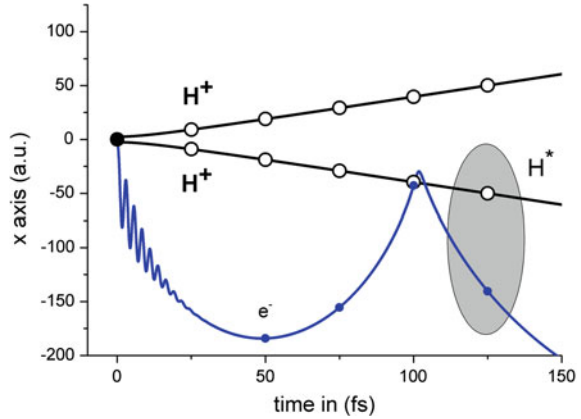


**Fig. 1.5** Sketch of the experimental set up, as described in the text. The detector shows a typical distribution of strong-field excited atoms

**Fig. 1.6** Sketch of the molecular FTI in  $\text{H}_2^+$ . The black dot designate the two protons initially located too close together to be resolved. See text for more explanation



### 1.3 Frustrated Tunneling Ionization in Strong-Field Fragmentation of Molecules

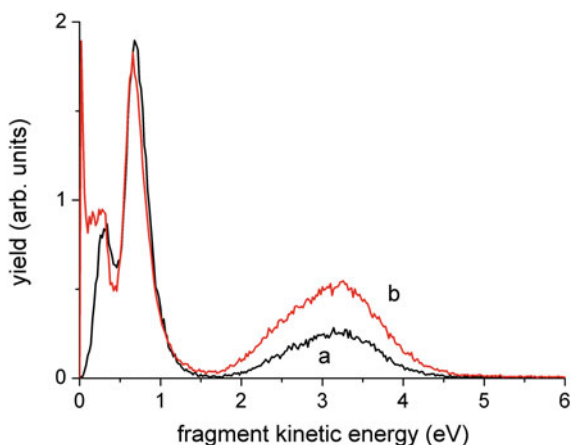
#### 1.3.1 Hydrogen Molecule

The process of frustrated tunneling ionization is not restricted to atoms but can also be observed in the strong-field dissociation of molecules [56], as first explored in  $\text{H}_2$ . The fragmentation of the simplest molecules  $\text{H}_2$  and  $\text{H}_2^+$  in strong laser fields has been well studied over the last decades. Fundamental fragmentation processes such as bond softening within the laser field and Coulomb explosion have been revealed [57]. Particularly, the process of Coulomb explosion, which is the repulsion of two protons, possible after the removal of the electrons in the strong field, can be exploited to study time and position dependent ionization [58]. The kinetic energy of the fragments gives detailed information on the nuclear distance at the instant of “ionization”. Since a tunneling process might precede both the fragmentation and also the Coulomb explosion, it is very tempting to investigate the fragmentation process in view of the FTI process.

To elucidate the physics, one can start by considering strong-field tunneling in the  $\text{H}_2^+$  molecular ion instead of the molecule. The scenario can be calculated by solving the coupled Newton equations for the three particles. One set of trajectories calculated for appropriate initial conditions is depicted in Fig. 1.6.

After tunneling the liberated electron quivers in the laser field sufficiently far away from the protons, so that it does not influence their acceleration process. After the laser pulse is over, the electron follows a trajectory that stays near one of the accelerated protons forming eventually an excited state of H. Consequently, the neutral fragment has virtually the same kinetic energy as the proton. In fact, starting from  $\text{H}_2$ , one can consider this process as Coulomb explosion without double ionization. Based on the detection method presented in Sect. 1.2.4, experiments become possible, where one

**Fig. 1.7** Kinetic energy distribution of ionic and excited neutral fragments after strong field interaction at an intensity of  $I = 3 \times 10^{14}$  W/cm<sup>2</sup>. Kinetic energy distribution of **a**  $H^+$  (black curve) and **b**  $H^*$  (red curve). From [56]



specifically detects excited neutral fragments from the strong-field fragmentation of  $H_2$  together with an ionic fragment spectrum. The detection of excited neutral fragments is facilitated by the fact that, owing to the high kinetic energy, the travel times towards the detector are substantially shorter than for excited atoms in an effusive beam. Consequently, the loss of excited atoms due to radiative decay to the ground state as in the atomic case is much less. In Fig. 1.7 the yield of excited neutral and charged fragments as a function of their kinetic energy is shown. As can be seen, both spectra are perfectly linked indicating that excited neutral fragments occur with the same kinetic energy as the charged ones. This obviously confirms that the Coulomb explosion involves finally a neutral excited state as sketched in Fig. 1.6. Moreover, also fragmentation processes such as the bond-softening, which are the origin of the peak at lower kinetic energy release (KER), are partially accompanied by FTI leading to low energy excited neutral fragments. To finally prove that the neutral fragments with high energy originate in a Coulomb explosion process, a coincidence measurement of the fast excited neutral and of the ionic fragment at 3 eV has been performed using a reaction microscope. The resulting correlated signal proves that both fragments stem from a single fragmentation process as suggested by the extended FTI model [56]. Comprehensive semiclassical calculations essentially confirm the validity of the picture [59, 60].

### 1.3.2 Small Molecules

The molecular FTI process is not restricted to the hydrogen molecule. The FTI process has also been confirmed to be in effect in the strong-field fragmentation of  $D_2^+$  [61]. Extensive experimental studies, in which the yields of excited fragments have been measured as a function of the laser intensity, the laser pulse duration and the laser polarization, reveal an overall satisfying modeling of the data within the

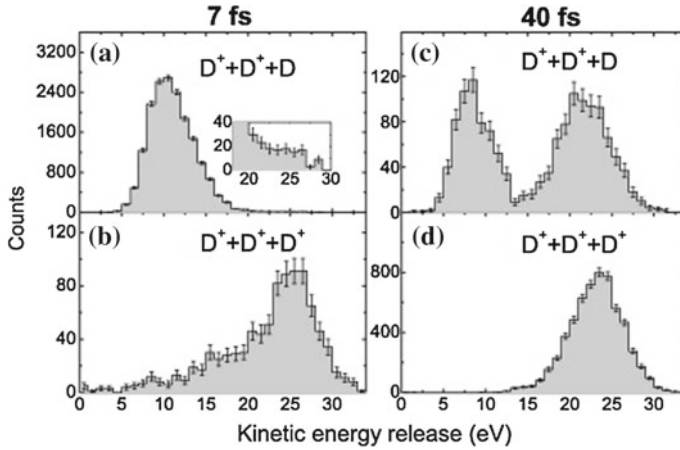


**Fig. 1.8** KER distributions for the three-body breakup of  $D_3^+$  at  $10^{16} \text{ W cm}^{-2}$ , 790 nm. Fragmentation with 7 fs pulses for **a**  $D^+ + D^+ + D$  and **b**  $D^+ + D^+ + D^+$  channels (inset of **(a)** shows an expanded vertical scale of the high-KER range). Fragmentation with 40 fs pulses for **c**  $D^+ + D^+ + D$  and **d**  $D^+ + D^+ + D^+$  channels. Note the high-KER feature between 15 and 30 eV in panel **(c)**, the main subject of discussion. From [63]

FTI process. An alternate process, namely re-collision excitation, has been discussed to possibly also contribute to excited fragments. However, it was concluded that it is by far not sufficient to explain the overall set of data.

Moreover, neutral excited fragments after strong-field dissociation have also been observed for  $N_2$  [62]. The  $N_2$  molecule provides a rich kinetic energy spectrum of fragments originating from many possible fragmentation channels involving single and also higher charged  $N^{n+}$  fragments. Analysis of the kinetic energy spectrum of excited neutrals shows that all fragmentation channels containing singly charged fragments allow for the FTI process. Based on this example one may conclude that the FTI process is a quite general phenomenon in strong-field dissociation of molecules.

Evidence of FTI in a polyatomic system has been found by the Kansas group, which studied the fragmentation process of  $D_3^+ \rightarrow D^+ + D^+ + D^*$  [63]. Surprisingly, at a laser intensity of  $10^{16} \text{ W cm}^{-2}$ , they observe high kinetic energy of the fragments that mimics the behavior of the  $D^+ + D^+ + D^+$  channel and which can be finally attributed to frustrated tunneling ionization, see Fig. 1.8. Furthermore, they also find evidence of FTI in both two-body and three-body break up. More elaborate calculations on the fragmentation process are performed by Lötstedt [64].

### 1.3.3 Dimers

Frustrated tunneling ionization works also in strong-field multiple ionization of loosely bound noble gas dimers, and has been specifically studied in  $Ar_2$  [65–69],

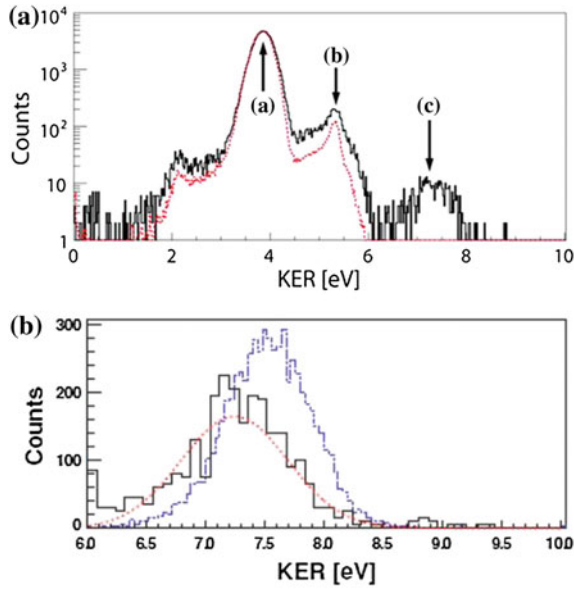


**Fig. 1.9** **a** The ion pair KER after strong-field double ionization of argon dimers at a laser pulse peak electric-field strength of 0.1 a.u. *Solid (black) line*, linear polarization; *dashed (red) line*, circular polarization of the laser beam, where the signal vanishes as expected for the FTI process (**a** similar spectrum is shown in [66]). **b** KER distribution for the Coulomb explosion channel  $\text{Ar}^{2+} + \text{Ar}^+$  after triple ionization of the  $\text{Ar}_2$  dimer [*dashed (blue) line*]. The spectrum was taken simultaneously with the corresponding KER spectrum for the Coulomb explosion channel  $\text{Ar}^+ + \text{Ar}^+$ , see (**a**). From [65]

where the FTI mechanism has been observed to be in effect in ionic fragments. Triple ionization of the  $\text{Ar}_2$  dimer, where altogether three electrons of the dimer (tunnel) ionize, leads to the Coulomb explosion of  $\text{Ar}^{2+}$  and  $\text{Ar}^+$  fragments with high kinetic energy. Rather than detecting a fast  $\text{Ar}^{2+}$  ion fragment, FTI of one of the electrons reduces the charge by unity by trapping the electron in an excited ionic Rydberg state. This is shown in Fig. 1.9a. The process is thus similar to FTI in  $\text{H}_2$ , but involves higher charge states, and rather than finding a neutral excited fragment the process results in an excited singly charged fragment. In Fig. 1.9b it is shown that the kinetic energy of the fragments in the FTI process is slightly reduced compared to the pure  $\text{Ar}^+ - \text{Ar}^+$  fragmentation channel providing information about the final  $n$  and  $l$  states populated in the excited fragment. Furthermore, frustrated tunneling ionization of two electrons have been postulated by [60]. This process has been observed and studied in Ar dimers [67]. Finally, in mixed and pure rare gas dimers the FTI process might initiate ion core charge oscillations, which eventually result in ionization of the populated Rydberg states giving rise to a specific low energy feature in the photoelectron spectrum [68, 69].

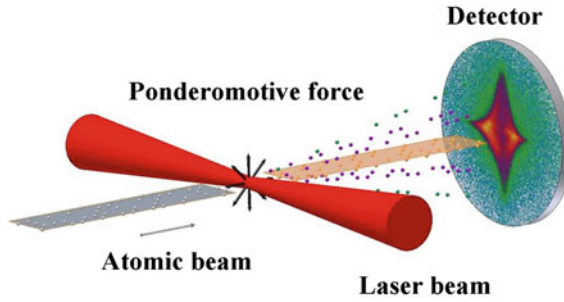


**Fig. 1.10** Influence of the ponderomotive force on the measured spatial distribution of strong-field excited atoms

## 1.4 Kinematic Effects on Atoms

### 1.4.1 Acceleration of Neutral Atoms in Strong Laser Fields

Gradient (dipole) forces acting on matter in the focus of a continuous wave laser field are well known and extensively exploited to trap macroscopic neutral particles (optical tweezer) or to confine cold quantum gases in light lattices [70]. In contrast to recoil forces, which are in effect, e.g., in laser cooling, and are also present in plane-wave fields, gradient forces are directly proportional to the light intensity gradient. Kinematic manipulation of neutral atoms in inhomogeneous laser fields is essentially based on the Lorentz force acting on a polarizable atomic system. The laser field causes only a minor perturbation and the static polarizability of the atom can be employed in the case that the laser photon energy is sufficiently below the excitation energy of the first excited state. In the course of the work on atomic excitation in strong laser fields, it turns out that a similar force acts on the surviving neutral atoms. In this case, however, the light intensities exceed the threshold intensity for ionization by far and constitute by no means a small perturbation.

In fact, using He atoms, a strong radial ponderomotive force (schematically indicated by the black arrows in Fig. 1.10b) was identified that accelerates the excited atoms with an unprecedented rate and causes a measurable radial deflection [71] despite the fact that the force acts only on extremely short times scales. We note that the intensity gradient in a focused laser beam is strongest in radial direction and negligible along the  $z$  direction, which is the propagation direction of the laser beam. The radial intensity gradient is strongest at the focal plane at half the beam spot size and drops symmetrically along the laser beam axis. It gives rise to a characteristic detection pattern. In Fig. 1.11 we show an experimental result, where the distribution of laser excited He atoms in a beam with a position sensitive detector located 0.3 m downstream from the interaction region was measured. The momentum transfer to the neutral atoms during the short interaction time is by far stronger than what one would expect from the dipole force acting on ground state atoms.

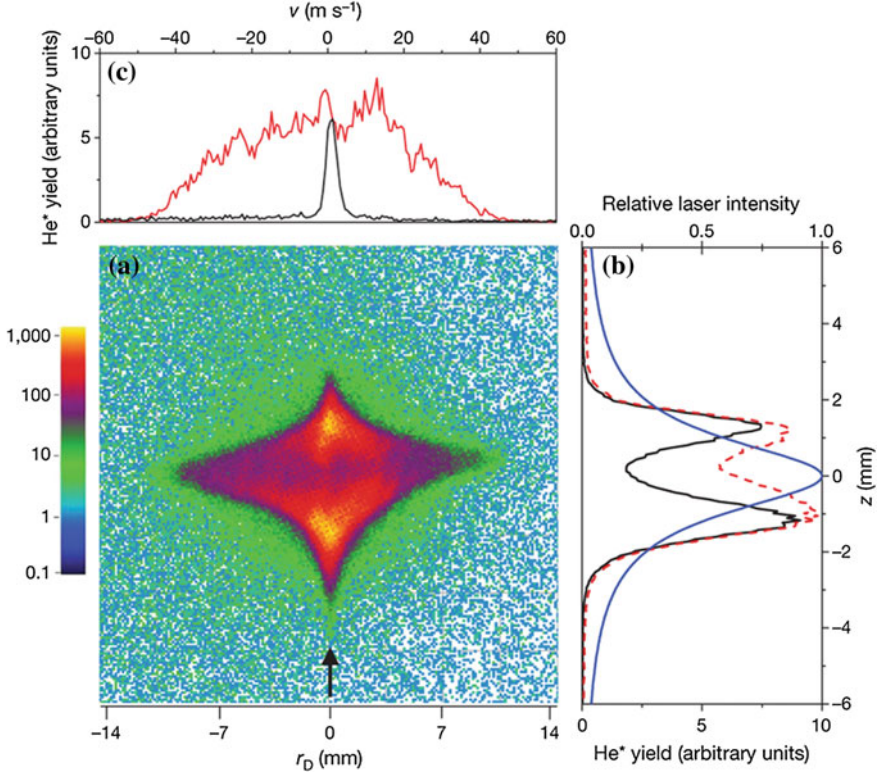


**Fig. 1.11** Deflection of neutral He atoms after interaction with a focused laser beam. **a** Distribution of excited He\* atoms on the detector. The laser beam direction is indicated by the arrow. **b** Cut through the atom distribution along the laser beam axis ( $z$  axis) at  $r_D = 0$  mm (black curve) and full projection on  $z$  axis (dashed red curve). Intensity along the  $z$  axis in units of the laser peak intensity  $I_0 = 6.9 \times 10^{15} \text{ W cm}^{-2}$  (blue curve). **c** Cuts through the distribution at  $z = 0$  mm (red curve) and  $z = -2.7$  mm (black curve). The black curve shows the velocity distribution of excited neutral atoms at a position unaffected by the ponderomotive force, showing quasi the “natural” velocity spread, while the red curve shows the velocity gain through the ponderomotive force. From [71]

The FTI picture helps to grasp the idea of how atomic acceleration proceeds in strong laser fields. We first recall that the ponderomotive force  $\mathbf{F}_p$  on a free electron (charged particle) exposed to an inhomogeneous electromagnetic field is given by

$$\mathbf{F}_p = -\frac{q^2}{2m\omega^2} \nabla |\mathbf{F}(\mathbf{r}, t)|^2, \quad (1.6)$$

Here,  $m$  and  $q$  are the mass and the charge of the particle, respectively, and the linearly polarized electric field now additionally depends on spatial coordinates  $\mathbf{F}(\mathbf{r}, t) = \mathbf{F}_0(\mathbf{r})f(t)\cos\omega t$ , with  $\mathbf{F}_0(\mathbf{r}) = F_0(\mathbf{r})\hat{\mathbf{e}}_x$ . Hence, transferred to the FTI model, we assume that the ponderomotive force due to the strong radial intensity gradient in

the focused laser field acts on the liberated electron, which quivers like a quasi free electron with a large amplitude at the laser frequency during the laser pulse. Important to note is that the ionic core is not affected by the ponderomotive force due to its large mass. Consequently, quiver energy of the electron is partially converted into center-of-mass (CM) motion of the whole atom. Since the ionic core and the electron are coupled by the Coulomb force and remain eventually bound, the whole atom is substantially accelerated. According to the FTI model one can rewrite (1.6) for the CM position  $\mathbf{R}$  of the neutral atom

$$M\ddot{\mathbf{R}}(t) = -\frac{e^2}{2m_e\omega^2} \nabla |\mathbf{F}(\mathbf{r}, \mathbf{t})|^2 \quad (1.7)$$

Here,  $M$  and  $m_e = 1$  a.u. are the masses of the atom and the electron, respectively. One can calculate the ponderomotive force for a linearly polarized laser beam with a Gaussian spatial intensity distribution, which reads in cylindrical coordinates

$$I(\mathbf{r}) = |\mathbf{F}_0(\mathbf{r})|^2 = I_0 \left( 1 + \left( \frac{z}{z_0} \right)^2 \right)^{-1} \exp \frac{-2r^2}{r_0^2}, \quad (1.8)$$

where  $r_0 = w_0 \sqrt{1 + \left( \frac{z}{z_0} \right)^2}$ ,  $w_0$  is the beam waist and  $I_0$  is the laser peak intensity. Evaluating the gradient in (1.7) with the intensity distribution given by (1.8) one obtains for the radial component  $r_c$  of the CM position perpendicular to the laser beam direction

$$\ddot{r}_c(t) = \frac{I(\mathbf{R})}{M\omega^2} \frac{r_c(t)}{r_0^2} f(t) \quad (1.9)$$

One may take  $f(t) = \exp(-t^2/\tau^2)$ , where  $\tau$  is the pulse width.

From (1.9) one finds that the maximum force along the radial direction scales as  $r_0^{-1}$ . Similarly, one can show that it scales as  $z_0^{-1}$  along the laser beam direction. Since the Rayleigh length  $z_0$  is typically a factor 100 larger than the beam waist  $r_0$ , the gradient and thus the ponderomotive force in laser beam direction is much smaller than in the radial direction and can be neglected. Assuming that the neutral atom does not move during the laser pulse, one can set  $r_c(t) = r_c$  on the right hand side of the equation. This allows one to solve (1.9) analytically for any initial position of an atom in the laser beam by just time integrating over laser pulse envelope. Considering the instant of tunneling with respect to the pulse envelope maximum,  $t_s$ , one obtains  $S(t_s) = \frac{\sqrt{\pi}\tau}{2} \text{erfc}(t_s/\tau)$ , where  $\text{erfc}$  denotes the complementary error function. Atoms located at half beam waist  $r_0/2$  experience the maximum force. The appropriate velocity  $v_{\max}(z)$  is given by

$$v_{\max}(z) = \frac{I_0}{2M\omega^2 w_0} \frac{\exp(-0.5)}{\sqrt{1 + \left(\frac{z}{z_0}\right)^2}^3} S(t_s) \quad (1.10)$$

Under the assumption that the initial tunneling process occurs early in the pulse, the experimental results agree very nicely with this formula. For He atoms exposed to a focused laser beam at maximum intensity ( $I = 7 \times 10^{15} \text{ W cm}^{-2}$ ) one obtains from the data a maximum velocity of about 55 m/s. This, in turn, results from an acceleration of about  $2 \times 10^{14} g$ , where  $g$  is Earth's acceleration. This is one of the highest direct acceleration rate of neutral atoms ever achieved.

In order to derive acceleration of the CM of the neutral atom within the FTI model without field cycle averaging the full coupled full Lorentz equations, including the magnetic field, for the ionic core and the electron need to be solved. Most important, one finds bound excited states with the CM velocity confirming basically the results of (1.10). Observed deflections for He and Ne atoms for different laser parameters are in very good agreement with simple theoretical predictions [71] and more extended calculations [72].

Finally, we mention, that the relatively weak intensity gradient, which is on the laser beam waist length scale, is not strong enough to change the electron dynamics on an atomic scale and the predicted  $n$  state distribution remains unchanged. This situation might change significantly, however, if one studies neutral atom acceleration in a short-pulse intense standing wave. The strong periodic intensity gradients on the scale of the laser wavelength might introduce non dipole effects in the electron dynamics. First results of this Kapitza-Dirac scattering of neutral He atoms in an intense standing wave indicates this [73].

### 1.4.2 Rydberg Atoms in Strong Laser Fields

From the experiments described before, one can infer that an atom surviving the interaction with a strong laser field carries information about the laser intensity it has interacted with. This twist has been exploited in an experiment studying the survival and ionization of Rydberg atoms in a strong laser field [74]. We note that the ionization of a Rydberg atom is expected to neither follow the picture of tunneling nor the picture of a multi-photon process. The very successful semi-classical Keldysh theory for strong-field ionization [1] and with it, the Keldysh parameter  $\gamma$ , are not applicable. Although Rydberg atoms are expected to be rather stable against ionization, experimental studies are scarce. The experimental setup is as follows: A Mach-Zehnder interferometer provides two time delayed laser pulses with different polarization and very good spatial overlap in the focus [75]. With the first linearly polarized strong laser pulse with an intensity of  $2.7 \times 10^{15} \text{ W cm}^{-2}$  a Rydberg wavepacket is excited in He and accelerated in the laser focus, as described before. After a time delay of 500 fs, a second elliptically polarized laser pulse (ellipticity  $\epsilon = 0.66$ ) with an intensity of  $3.8 \times 10^{15} \text{ W cm}^{-2}$  is applied. As outlined in

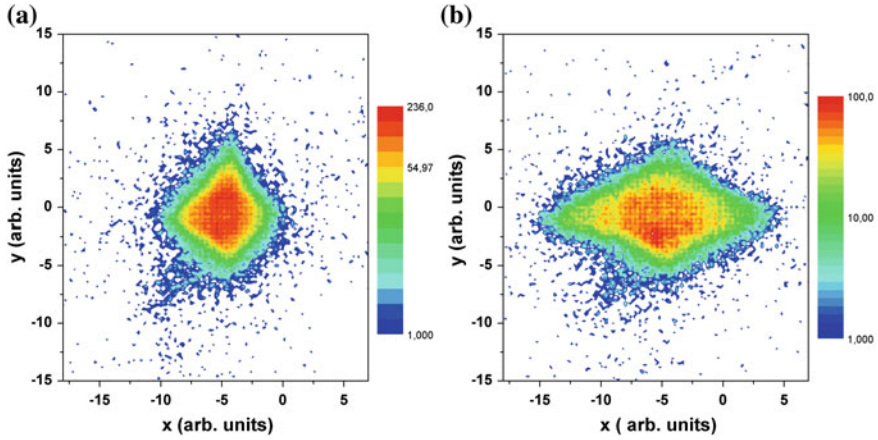


**Fig. 1.12** **a** Excitation of He Rydberg atoms and deflection after interaction with a linearly polarized laser field,  $I = 2.7 \times 10^{15} \text{ W cm}^{-2}$ . **b** Interaction of the produced Rydberg population with an elliptically polarized laser,  $I = 3.8 \times 10^{15} \text{ W cm}^{-2}$ ,  $\epsilon = 0.66$

Sect. 1.2.2, sufficient elliptical polarization ensures that no further excitation from the ground state takes place [15]. Consequently, any Rydberg atom, that interacts with the second laser pulse and survives it, is additionally accelerated, provided, it is located in a nonzero intensity gradient. Hence, the deflection of Rydberg atoms, which can be measured as described before, verifies the interaction with the strong laser field.

We show the measured deflection of the Rydberg atoms excited by the first laser pulse in Fig. 1.12a. Figure 1.12b displays Rydberg atoms surviving the second laser pulse, which also accelerates them additionally. It has been found that the detected population after the second pulse drops at most by 15 % indicating for the first time an experimental proof of the exceptional stability of Rydberg atoms at laser intensities above  $10^{15} \text{ W cm}^{-2}$ . This means that the Rydberg atoms withstand corresponding field amplitudes of more than 1 GV/cm, which exceed the thresholds for static-field ionization by more than six orders of magnitude. Further analysis reveals that Rydberg atoms are predominantly excited within a radius half of the focus size  $w_0/2$  of the second laser pulse. For this regime there is a unique relation between deflection of the atom and the intensity it has interacted with. Thus, surviving atoms have seen 60–95 % of the maximum intensity of the second pulse. As a result of quantum mechanical calculations, mainly low order processes are in effect, even at highest intensities. However, the calculations show important deviations from simple low-order perturbation theory at intensities, where the quiver amplitude is comparable or larger than the classical inner turning point of the Rydberg orbit. Finally, we remark that the high survival rate can be fruitfully exploited to steer neutral atoms by varying the spatial overlap of the two laser pulses, which breaks the radial symmetry of the field gradient [76].

## 1.5 Summary and Outlook

In conclusion we describe the process of frustrated tunneling ionization (FTI), a recently found new exit channel in the strong-field tunneling-plus-rescattering model that leads to the population of excited states, if the Coulomb field is taken into account explicitly. The FTI process allows for a qualitative and, even more important, also for a quantitative understanding of how excitation proceeds in the tunneling regime of strong-field physics. We demonstrate the ubiquity of FTI in strong-field physics by presenting various examples in atomic and molecular strong-field dynamics and dissociation. In all cases the concept of FTI facilitates the comprehension of observed phenomena. Furthermore, FTI also grants access to the understanding of acceleration of surviving excited atoms in spatially non-uniform strong laser fields such as a single focused laser field or two overlapping co- and counter-propagating laser fields. Observation of the resulting atomic deflection becomes possible by exploiting a position sensitive detection scheme for neutral excited atoms. This enables one to test the stability of Rydberg atoms in strong laser fields, where the experiment not only proves the high survival rate of Rydberg states, but also show unambiguously that the information, which intensity a Rydberg atom has survived, is encoded in its kinematics.

Future experiments on atomic and molecular excitation and acceleration will rely on and benefit from newly available laser sources in the mid infrared range. Particularly interesting is to study whether the interplay of stronger ponderomotive forces and the modified bound state formation through the strong acceleration and large excursion of the electron (non-dipole effects) leads to stronger neutral atomic acceleration. Furthermore, investigation of bound state formation in H-like and He-like ions is suited to explore the limits of the frustrated tunneling ionization model at higher laser intensities.

**Acknowledgments** The author thanks W. Becker, S. Eilzer, T. Nubbemeyer, H. Rottke, A. Saenz, W. Sandner, H. Reiss, and H. Zimmermann for fruitful discussions.

## References

1. L.V. Keldysh, Sov. Phys. JETP **20**, 1307 (1965)
2. H.B. van Linden van den Heuvell, H.G. Muller, in *Multiphoton Processes*, ed. by S.J. Smith, P.L. Knight (Cambridge University Press, Cambridge, 1988)
3. T.F. Gallagher, Phys. Rev. Lett. **61**, 2304 (1988)
4. P.B. Corkum, N.H. Burnett, F. Brunel, Phys. Rev. Lett. **62**, 1259 (1989)
5. P.B. Corkum, Phys. Rev. Lett. **71**, 1994 (1993)
6. K.C. Kulander, K.J. Schafer, J.L. Krause, *Super-Intense Laser-Atom Physics* (Plenum, New York, 1993)
7. K.J. Schafer, B. Yang, L.F. DiMauro, K.C. Kulander, Phys. Rev. Lett. **70**, 1599 (1993)
8. G.G. Paulus, W. Nicklich, H. Xu, P. Lambropoulos, H. Walther, Phys. Rev. Lett. **72**, 2851 (1994)

9. B. Walker, B. Sheehy, L.F. DiMauro, P. Agostini, K.J. Schafer, K.C. Kulander, *Phys. Rev. Lett.* **73**, 1227 (1994)
10. R. Moshhammer, B. Feuerstein, W. Schmitt, A. Dorn, C.D. Schröter, J. Ullrich, H. Rottke, C. Trump, M. Wittmann, G. Korn, K. Hoffmann, W. Sandner, *Phys. Rev. Lett.* **84**, 447 (2000)
11. T. Weber, M. Weckenbrock, A. Staudte, L. Spielberger, O. Jagutzki, V. Mergel, F. Afaneh, G. Urbasch, M. Vollmer, H. Giessen, R. Dörner, *Phys. Rev. Lett.* **84**, 443 (2000)
12. W. Becker, X. Liu, P.J. Ho, J.H. Eberly, *Rev. Mod. Phys.* **84**, 1011 (2012)
13. M. Lewenstein, P. Balcou, M.Y. Ivanov, A. L'Huillier, P.B. Corkum, *Phys. Rev. A* **49**, 2117 (1994)
14. F. Krausz, M. Ivanov, *Rev. Mod. Phys.* **81**, 163 (2009)
15. T. Nubbemeyer, K. Gorling, A. Saenz, U. Eichmann, W. Sandner, *Phys. Rev. Lett.* **101**, 233001 (2008)
16. M.P. de Boer, H.G. Muller, *Phys. Rev. Lett.* **68**, 2747 (1992)
17. M.P. de Boer, L.D. Noordam, H.G. Muller, *Phys. Rev. A* **47**, R45 (1993)
18. R.R. Jones, D.W. Schumacher, P.H. Bucksbaum, *Phys. Rev. A* **47**, R49 (1993)
19. L. Dimauro, P. Agostini, *Adv. At. Mol. Opt. Phys.* **35**, 79 (1995)
20. R.R. Freeman, P.H. Bucksbaum, H. Milchberg, S. Darack, D. Schumacher, M.E. Geusic, *Phys. Rev. Lett.* **59**, 1092 (1987)
21. A. Scrinzi, N. Elander, B. Piroux, *Phys. Rev. A* **48**, R2527 (1993)
22. M.V. Fedorov, A. Movsesian, *J. Phys. B: At. Mol. Opt. Phys.* **21**, L155 (1988)
23. R.R. Jones, P.H. Bucksbaum, *Phys. Rev. Lett.* **67**, 3215 (1991)
24. L.D. Noordam, H. Stapelfeldt, D.I. Duncan, T.F. Gallagher, *Phys. Rev. Lett.* **68**, 1496 (1992)
25. J.G. Story, D.I. Duncan, T.F. Gallagher, *Phys. Rev. Lett.* **70**, 3012 (1993)
26. J.H. Hoogenraad, R.B. Vrijen, L.D. Noordam, *Phys. Rev. A* **50**, 4133 (1994)
27. O.V. Tikhonova, E.A. Volkova, A.M. Popov, M.V. Fedorov, *Phys. Rev. A* **60**, R749 (1999)
28. F. Benvenuto, G. Casati, D.L. Shepelyansky, *Phys. Rev. A* **45**, R7670 (1992)
29. W.C. Henneberger, *Phys. Rev. Lett.* **21**, 838 (1968)
30. M. Pont, N.R. Walet, M. Gavrila, C.W. McCurdy, *Phys. Rev. Lett.* **61**, 939 (1988)
31. K.C. Kulander, K.J. Schafer, J.L. Krause, *Phys. Rev. Lett.* **66**, 2601 (1991)
32. J.H. Eberly, K.C. Kulander, *Science* **262**, 1229 (1993)
33. M. Gavrila, *J. Phys. B: At. Mol. Opt. Phys.* **35**, R147 (2002)
34. A.M. Popov, O.V. Tikhonova, E.A. Volkova, *J. Phys. B: At. Mol. Opt. Phys.* **36**, R125 (2003)
35. F. Morales, M. Richter, S. Patchkovskii, O. Smirnova, *Proc. Nat. Acad. Sci.* **108**, 16906 (2011)
36. M. Richter, S. Patchkovskii, F. Morales, O. Smirnova, M. Ivanov, *New J. Phys.* **15**, 083012 (2013)
37. M.P. de Boer, J.H. Hoogenraad, R.B. Vrijen, L.D. Noordam, H.G. Muller, *Phys. Rev. Lett.* **71**, 3263 (1993)
38. N.J. van Druten, R.C. Constantinescu, J.M. Schins, H. Nieuwenhuize, H.G. Muller, *Phys. Rev. A* **55**, 622 (1997)
39. E. Wells, I. Ben-Itzhak, R.R. Jones, *Phys. Rev. Lett.* **93**, 023001 (2004)
40. A. Talebpour, C.Y. Chien, S.L. Chin, *J. Phys. B: At. Mol. Opt. Phys.* **29**, 5725 (1996)
41. M. Gajda, J. Grochmalicki, M. Lewenstein, K. Rzażewski, *Phys. Rev. A* **46**, 1638 (1992)
42. G.L. Yudin, M.Y. Ivanov, *Phys. Rev. A* **63**, 033404 (2001)
43. H.G. Muller, *Phys. Rev. Lett.* **83**, 3158 (1999)
44. N. Shvetsov-Shilovski, S. Goreslavski, S. Popruzhenko, W. Becker, *Laser Phys.* **19**, 1550 (2009)
45. N.B. Delone, V.P. Krainov, *J. Opt. Soc. Am. B* **8**, 1207 (1991)
46. D. Comtois, D. Zeidler, H. Pepin, J.C. Kieffer, D.M. Villeneuve, P.B. Corkum, *J. Phys. B: At. Mol. Opt. Phys.* **38**, 1923 (2005)
47. K. Huang, Q. Xia, L. Fu, *Phys. Rev. A* **87**, 033415 (2013)
48. S. Chen, X. Gao, J. Li, A. Becker, A. Jaron Becker, *Phys. Rev. A* **86**, 013410 (2012)
49. E. Volkova, A. Popov, O. Tikhonova, *J. Exp. Theor. Phys.* **113**, 394 (2011)
50. T. Morishita, C.D. Lin, *Phys. Rev. A* **87**, 063405 (2013)
51. Q. Li, X.M. Tong, T. Morishita, H. Wei, C.D. Lin, *Phys. Rev. A* **89**, 023421 (2014)
52. H. Zimmermann, J. Buller, S. Eilzer, U. Eichmann, *Phys. Rev. Lett.* **114**, 123003 (2015)

53. A.S. Landsman, A.N. Pfeiffer, C. Hofmann, M. Smolarski, C. Cirelli, U. Keller, *New J. Phys.* **15**, 013001 (2013)
54. A.T.J.B. Eppink, D.H. Parker, *Rev. Sci. Instrum.* **68**, 3477 (1997)
55. R. Dörner, V. Mergel, O. Jagutzki, L. Spielberger, J. Ullrich, R. Moshhammer, H. Schmidt-Böcking, *Phys. Rep.* **330**, 95 (2000)
56. B. Manschwetus, T. Nubbemeyer, K. Gorling, G. Steinmeyer, U. Eichmann, H. Rottke, W. Sandner, *Phys. Rev. Lett.* **102**, 113002 (2009)
57. J.H. Posthumus, *Rep. Progr. Phys.* **67**, 623 (2004)
58. S. Chelkowski, P.B. Corkum, A.D. Bandrauk, *Phys. Rev. Lett.* **82**, 3416 (1999)
59. A. Emmanouilidou, C. Lazarou, A. Staudte, U. Eichmann, *Phys. Rev. A* **85**, 011402 (2012)
60. A. Emmanouilidou, C. Lazarou, *New J. Phys.* **14**, 115010 (2012)
61. J. McKenna, S. Zeng, J.J. Hua, A.M. Sayler, M. Zohrabi, N.G. Johnson, B. Gaire, K.D. Carnes, B.D. Esry, I. Ben-Itzhak, *Phys. Rev. A* **84**, 043425 (2011)
62. T. Nubbemeyer, U. Eichmann, W. Sandner, *J. Phys. B: At. Mol. Opt. Phys.* **42**, 134010 (2009)
63. J. McKenna, A.M. Sayler, B. Gaire, N.G. Kling, B.D. Esry, K.D. Carnes, I. Ben-Itzhak, *New J. Phys.* **14**, 103029 (2012)
64. E. Lötstedt, T. Kato, K. Yamanouchi, *Phys. Rev. Lett.* **106**, 203001 (2011)
65. B. Manschwetus, H. Rottke, G. Steinmeyer, L. Foucar, A. Czasch, H. Schmidt-Böcking, W. Sandner, *Phys. Rev. A* **82**, 013413 (2010)
66. B. Ulrich, A. Vredenburg, A. Malakzadeh, M. Meckel, K. Cole, M. Smolarski, Z. Chang, T. Jahnke, R. Dörner, *Phys. Rev. A* **82**, 013412 (2010)
67. J. Wu, A. Vredenburg, B. Ulrich, L.P.H. Schmidt, M. Meckel, S. Voss, H. Sann, H. Kim, T. Jahnke, R. Dörner, *Phys. Rev. Lett.* **107**, 043003 (2011)
68. A. von Veltheim, B. Manschwetus, W. Quan, B. Borchers, G. Steinmeyer, H. Rottke, W. Sandner, *Phys. Rev. Lett.* **110**, 023001 (2013)
69. M. Li, H. Liu, C. Wu, Y. Deng, C. Wu, Q. Gong, Y. Liu, *Phys. Rev. A* **89**, 025402 (2014)
70. R. Grimm, M. Weidemüller, Y.B. Ovchinnikov, *Adv. At. Mol. Opt. Phys.* **42**, 95 (2000)
71. U. Eichmann, T. Nubbemeyer, H. Rottke, W. Sandner, *Nature* **461**, 1261 (2009)
72. Q.Z. Xia, L.B. Fu, J. Liu, *Phys. Rev. A* **87**, 033404 (2013)
73. S. Eilzer, H. Zimmermann, U. Eichmann, *Phys. Rev. Lett.* **112**, 113001 (2014)
74. U. Eichmann, A. Saenz, S. Eilzer, T. Nubbemeyer, W. Sandner, *Phys. Rev. Lett.* **110**, 203002 (2013)
75. T. Nubbemeyer, U. Eichmann, *Eur. Phys. J. Spec. Top.* **222**, 2267 (2013)
76. S. Eilzer, U. Eichmann, *J. Phys. B: At. Mol. Opt. Phys.* **47**, 204014 (2014)

Ultrafast Dynamics Driven by Intense Light Pulses

From Atoms to Solids, from Lasers to Intense X-rays

Kitzler, M.; Gräfe, S. (Eds.)

2016, XX, 379 p. 159 illus., 87 illus. in color., Hardcover

ISBN: 978-3-319-20172-6